The Dynamics of Binary Neutron Star Mergers and GW170817

David Radice,[1,2,3] Sebastiano Bernuzzi,[4] and Albino Perego[5,6]

[1]Institute for Gravitation and the Cosmos, The Pennsylvania State University, University Park, Pennsylvania 16802, USA; email: david.radice@psu.edu

[2]Department of Physics, The Pennsylvania State University, University Park, Pennsylvania 16802, USA

[3]Department of Astronomy & Astrophysics, The Pennsylvania State University, University Park, Pennsylvania 16802, USA

[4]Theoretisch-Physikalisches Institut, Friedrich-Schiller-Universität Jena, 07743 Jena, Germany

[5]Dipartimento di Fisica, Universitá di Trento, I-38123 Trento, Italy

[6]INFN-TIFPA, Trento Institute for Fundamental Physics and Applications, I-38123 Trento, Italy

Keywords

neutron stars, gravitational wave generation, gravitational wave sources, multimessenger astrophysics

Abstract

With the first observation of a binary neutron star merger through gravitational waves and light, GW170817, compact binary mergers have now taken the center stage in nuclear astrophysics. They are thought to be one of the main astrophysical sites of production of r-process elements, and merger observations have become a fundamental tool to constrain the properties of matter. Here, we review our current understanding of the dynamics of neutron star mergers in general and of GW170817 in particular. We discuss the physical processes governing the inspiral, merger, and postmerger evolution, and we highlight the connections between these processes, the dynamics, and the multimessenger observables. Finally, we discuss open questions and issues in the field and the need to address them through a combination of better theoretical models and new observations.

Contents

1. INTRODUCTION

Neutron star (NS) mergers are at the heart of some of the most pressing problems in nuclear astrophysics. Binary systems composed of two NSs [binary neutron stars (BNSs)] have provided the first evidence for the existence of gravitational waves (GWs). The detection of a BNS merger (GW170817) by LIGO/Virgo and electromagnetic (EM) observer partners had a profound impact on our understanding of gravity, the physics of dense matter, the origin of short γ-ray bursts (SGRBs), and the site of production of r-process elements (1–3). Many more multimessenger observations of NS mergers are expected in the next years as the ground-based laser-interferometer detectors LIGO and Virgo reach their design sensitivity and as KAGRA and LIGO India join the network (4).

GW observation of inspiraling NSs can be used to measure the tidal deformability of the stars, probe the interior structure of NSs, and constrain the nature of matter at supernuclear densities (5–7). With third-generation detectors, or for rare very nearby events, it will be possible to observe GWs emitted by the merger product of two NSs possibly constraining the presence of phase transitions at several times nuclear densities and temperatures of tens of MeV (8–11).

NS mergers [NS–NS and NS–black hole (BH) mergers] are also thought to be an important, if not a dominant, astrophysical site of production of r-process elements, such as gold (12). The fact that NS mergers produce some r-process nuclei is now firmly established by the multimessenger observations of GW170817 (12). However, it is not clear whether NS mergers produce all the r-process nuclei or whether other astrophysical phenomena are required to explain the observed chemical abundances in our galaxy and satellites.

Isolated NSs are characterized by strong but stationary gravitational fields. Their self-gravity (or compactness $C_A = GM_A/c^2 R_A \sim 0.15$, with A labeling one of the NSs) cannot be neglected. BNS systems lose orbital angular momentum because of the emission of GWs, so BNS spacetimes are dynamical. Nevertheless, the evolution of close circularized binaries can still be considered as an adiabatic process as long as the radiation-reaction timescale is much longer than the orbital period. In particular, the inspiral can be well described by a sequence of circular orbits until shortly before merger. As the two NSs approach each other, finite size (tides) and hydrodynamic effects become progressively more relevant, and the inspiral terminates when the binary reaches the mass-shedding limit (Roche lobe overflow) (13).

Simulations in numerical relativity (NR) are the most appropriate tool to study the dynamical phases of BNS mergers: the late inspiral (the last $\sim$20 orbits), the merger, and its aftermath.

Sophisticated models are required to quantitatively study all the features related to the merger and postmerger phase. State-of-the-art simulations include dynamically evolving space-time; finite-temperature, composition-dependent nuclear equation of state (EoS); general-relativistic magnetohydrodynamics (GRMHD); weak interactions; and neutrino transport, although with different levels of approximations (see, e.g., 14–21).

In this review, we discuss the dynamics of BNS mergers: their qualitative and quantitative features, the physics that controls the evolution of the binary, and the multimessenger signatures of the dynamics. Particular emphasis is on the nuclear astrophysics implications of mergers and on the comparison between theoretical predictions and GW170817, as well as on the new questions raised by the first detection. For a more general overview of NS mergers, we refer readers to Reference 22. For more detailed discussion of the EM emissions from BNS mergers, we refer readers to References 23–25. The recent review by Shibata & Hotokezaka (26) discusses mass ejection from NS mergers in detail and is complementary to ours. We focus on the connection between outflow properties and specific physical processes and features of the postmerger dynamics.

The rest of this review is organized as follows. Section 2 discusses the inspiral phase with emphasis on the physics of the two-body problem in general relativity (GR) and on tidal effects. Section 3 discusses the merger and postmerger evolution. We introduce physical processes operating in these phases and the associated timescales, and we discuss the outcomes of mergers and of GW170817. Section 4 is dedicated to the discussion of mass ejection from BNS mergers and how the features of the outflow depend on the postmerger dynamics. We conclude with a summary of key points and open questions in the field.

2. NEUTRON STARS INSPIRAL

If a binary forms through standard formation channels (4), eccentricity is efficiently radiated during the early evolution, and by the time the binary enters the frequency band of ground-based GW interferometers, the motion is circularized. Then the stars inspiral toward each other for the last few minutes (thousands of orbits) of evolution emitting a GW signal that increases in amplitude and frequency (chirp) until it reaches a maximum, conventionally denoted as the moment of merger.

2.1. Two-Body Dynamics

The quasi-circular and quasi-adiabatic inspiral motion can be described within the post-Newtonian (PN) approximation to general relativity (27). The PN approximation applies to strongly self-gravitating compact binaries when the bodies are well separated and the orbital angular velocity Ω is small, because it is an expansion in the relative velocity v/c, which is formally valid only if $v/c \ll 1$. The motion is characterized by an adiabaticity parameter $\dot{\Omega}/\Omega^2 \ll 1$, which indicates that the radiation-reaction timescale is longer than the orbital timescale.

The predicted gravitational signal is, at leading order, emitted at a frequency twice the orbital frequency with amplitude and phase scaling given by (quadrupole formula)

$$h(t) \sim \frac{1}{d}\mathcal{M}_c^{5/3} f_{GW}^{2/3} = v\frac{M}{d}(Mf_{GW}(t))^{2/3}, \quad \phi(t) \sim 2\mathcal{M}_c^{-5/8} t^{5/8} = 2v^{-3/8}(t/M)^{5/8}, \qquad 1.$$

where $\mathcal{M}_c = Mv^{3/5}$ (chirp mass), $M = M_A + M_B$ (binary mass), $v = M_A M_B/M^2$ (symmetric mass ratio), $f_{GW} = \dot{\phi}$, d is the source distance, and, for clarity, we have suppressed geometric factors and assumed that $G = c = 1$. Note that the problem trivially scales with the total mass M of the

system as long as the bodies can be considered point-masses; this holds in general and also for binary BHs (BBHs). Tidal interactions due to the finite size of the bodies are effects that formally enter the action at fifth PN order. As discussed below, the BNS dynamics is influenced by the tidal interactions of the two stars at the frequencies relevant for ground-based detector observations.

The PN approach qualitatively describes the inspiral phase, but because PN is an asymptotic expansion, it ultimately fails to quantitatively describe binaries in the high-frequency regime (i.e., $f_{GW} \gtrsim 50$ Hz). The effective-one-body (EOB) is a formalism to solve the GR two-body problem that can be applied to both the low- and the high-velocity regimes (28). The EOB is a relativistic generalization of the well-known Newtonian property that the relative motion is equivalent to the motion of a particle of mass $\mu = \nu M$ in an effective potential. The GR dynamics can, in fact, be mapped into the motion of an effective particle μ in an effective metric. The EOB is a Hamiltonian formalism that semianalytically describes the inspiral–merger–ringdown dynamics of BBHs; Damour & Nagar (29) incorporated the treatment of tidal effect into the formalism, thus extending the model's applicability to BNS. For a review, readers are referred to Reference 30; here, we recall that EOB is a unified framework to incorporate different perturbation approaches to the two-body problem, re-sum the PN series, and include nonperturbative information from simulations.

2.2. Tidal Effects

The description of tidal interactions in the PN dynamics of self-gravitating and deformable bodies (31) was formulated in a series of works by Damour, Soffel and Xu in the 1990s (e.g., 32). They developed a multichart approach whereby an outer problem, in which the bodies are "skeletonized" as world lines with global properties, is matched to an inner problem, in which the effects of the other bodies in the world tube around a given body are included. In the case of compact binaries, the inner problem corresponds to the description of the tidal response of an NS due to the external gravitational field of the companion. The matching with the outer problem allows one to include the effect of the tidal deformations on the orbital dynamics and the GW radiation. The presentation here closely follows that of Damour & Nagar (29, 33).

A fully relativistic treatment of the inner problem was developed in References 33–35. In the local frame of body A, the internally generated mass M_L^A and spin S_L^A multipole moments, with $L = i_1 i_2 \ldots i_\ell$ being a multi-index, are related to the external gravitoelectric G_L^A and gravitomagnetic H_L^A tidal moments[1] by the tidal polarizability coefficients

$$M_L^A = \mu_\ell G_L^A, \quad S_L^A = \sigma_\ell H_L^A. \qquad 2.$$

The gravitoelectric (gravitomagnetic) coefficient $G\mu_l$ has dimension $[\text{length}]^{2\ell+1}$ and measures the ℓ-th-order mass (spin) multipolar moment induced in the NS by the external ℓ-th-order gravitoelectric (gravitomagnetic) field. The dimensionless relativistic Love numbers are defined as

$$k_\ell = \frac{(2\ell-1)!!}{2} \frac{G\mu_\ell}{R^{2\ell+1}}, \quad j_\ell = \frac{(2\ell-1)!!}{2} \frac{G\sigma_\ell}{R^{2\ell+1}}, \qquad 3.$$

with R being the NS radius. Note that many works in the literature focus on the dominant quadrupole $\ell = 2$ gravitoelectric coefficient and drop the subscript (e.g., 34). For BHs, $\mu_\ell^{BH} = \sigma_\ell^{BH} = 0$ (33, 35).

---

[1]The tidal moments are defined as the symmetric trace–free projection of the derivatives of the externally generated parts of the local gravitoelectric, $\bar{E}_a$, and gravitomagnetic, $\bar{B}_a$, fields—for instance, $G_L^A = \partial_{\langle L-1} \bar{E}_{a_\ell}^A \rangle|_{X^a \to 0}$, where X^a are local coordinates (33).

In practice, the calculation of the Love numbers reduces to the solution of stationary perturbations of spherical relativistic stars because it is assumed that the external field varies sufficiently slowly (adiabatic tides). The tidal coefficients have a strong dependency on the NS compactness. Thus, Love numbers must be computed in GR, not in the Newtonian limit. Love numbers depend on the EoS employed to construct the equilibrium NS. Hence, they carry the imprint of the EoS on the binary dynamics.

If the external field is dynamical, the star response can be described, at linear order in the deformation, as a superposition of the star's proper modes. Modes are excited when the orbital frequency matches their resonant frequency. The problem has been studied extensively in Newtonian gravity, in GR for a test mass orbiting an NS, and for comparable masses in PN theory (e.g., 36–38). Such dynamical tides are dominated by the fundamental pressure modes (f-modes), but typically in a nonresonant way because the f-modes' resonance is approximately in the kilohertz regime, which would correspond to the merger and postmerger phases, past the point where the stars exist as separate objects. Resonances can be excited for other types of modes (e.g., g-modes or r-modes) because these have lower frequencies, but their energies are smaller.

Finite-sized effects are incorporated into the PN two-body dynamics by augmenting the effective action

$$S = S_{\mathrm{GR}} + S_{\mathrm{pointmass}} = \frac{1}{16\pi G} \int R\sqrt{|g|}\mathrm{d}x - \sum_A \int M_A \mathrm{d}s_A, \qquad 4.$$

the second term being the skeletonized description as point masses, with the nonminimal (worldline) couplings

$$S_{\mathrm{nonminimal}} = \sum_A \frac{\mu_\ell^A}{2\ell!} \int (G_L^A)^2 \mathrm{d}s_A + \frac{\ell\,\sigma_\ell^A}{\ell!2(\ell+1)} \int (H_L^A)^2 \mathrm{d}s_A. \qquad 5.$$

The additional terms alter the dynamics at 5PN in a way that is linear in the tidal deformations. The tidal contribution to the two-body Lagrangian at leading PN (Newtonian) order contains only the $\ell = 2$ gravitoelectric terms and reads

$$L_{\mathrm{tidal}}^{\mathrm{LO}} = k_2^A GM_B^2 \frac{R_A^5}{r^6} + (A \leftrightarrow B), \qquad 6.$$

where r is the separation between the stars in the binary. Equation 6 indicates that tidal corrections are attractive and short range. The effect of tides can be illustrated considering the modification to the Kepler law given by the quadrupolar gravitoelectric term

$$\Omega^2 r^3 = GM\left[1 + 12\frac{M_A}{M_B}\frac{R_A^5}{r^5}k_2^A + (A \leftrightarrow B)\right]. \qquad 7.$$

At a given radius, the frequency is higher if the tidal interactions are present. In other words, the motion is accelerated by tidal effects, and the system merges earlier and at a lower frequency. The contact GW frequency of the two NSs can be estimated setting $r = R_A + R_B$ and finding $2GM\Omega \simeq 2(M_B/(MC_B) + M_B/(MC_B))^{-3/2}$ (29). For equal masses, the latter relation translates to

$$f_{\mathrm{GW}}^{\mathrm{contact}} \simeq 1.327 \left(\frac{C}{0.15}\right)^{3/2} \left(\frac{M}{2.8M_\odot}\right) \mathrm{kHz}. \qquad 8.$$

Simulations show that the contact between the two NSs happens approximately two to four GW cycles before merger at an even lower frequency $f_{\mathrm{GW}}^{\mathrm{NR,contact}} \simeq 700\,(M/2.8M_\odot)$ Hz (39).

The EOB two-body Hamiltonian for nonspinning binaries is written in terms of an effective Hamiltonian:

$$H_{\text{EOB}} = M\sqrt{1 + 2\nu(\hat{H}_{\text{eff}} - 1)}, \quad \hat{H}_{\text{eff}} = \frac{H_{\text{eff}}}{\mu} = \sqrt{A(u; \nu)(1 + p_\phi^2 u^2 + 2\nu(4 - 3\nu)u^2 p_{r*}^4) + p_{r*}^2}, \quad 9.$$

where $u = GM/rc^2$ is the Newtonian potential. The effective Hamiltonian H_{eff} reduces to the Hamiltonian of a particle in Schwarzschild space-time for $\nu \to 0$ where $A(u; 0) = 1 - 2u$. For finite mass ratio, the function $A(u; \nu)$ is computed from PN results, and it is completely known analytically up to 4PN (40).

For the point-particle dynamics, only some of the point-particle terms are known at 5PN. The expression at 4PN is remarkably simple:

$$A_0 = 1 - 2u + \nu(2u^3 + a_4 u^4 + a_5(\nu, \ln u)u^5), \quad 10.$$

where $a_4 = (94/3 - 41/32\pi)$, and $a_5(\nu, \ln u)$ is a linear function of ν and $\ln u$. For BBH applications, the function A_0 is further re-summed using analytical techniques (e.g., Padé functions), and the 5PN parameters that are not known analytically are fixed using NR results. Tidal interactions are included by augmenting the potential $A = A_0 + A_{\text{tidal}}$, with an expression inferred from the above tidal Lagrangian (41). The tidal potential has the form

$$A_{\text{tidal}} = \sum_{\ell \geq 2} \left[\kappa_\ell^{A+} u^{2\ell+2}(1 + \alpha_1^{(\ell+)}u + \alpha_2^{(\ell+)}u^2 + \ldots) + \kappa_\ell^{A-} u^{2\ell+3}(1 + \alpha_1^{(\ell-)}u + \ldots) + (A \leftrightarrow B) \right], \quad 11.$$

where $\alpha_i^{(\ell)}(\nu)$ are coefficients and

$$\kappa_\ell^{A+} = 2k_\ell^A \left(\frac{M_A}{MC_A} \right)^{2\ell+1} \frac{M_B}{M_A}, \quad \kappa_\ell^{A-} = 2j_\ell^A \left(\frac{M_A}{MC_A} \right)^{2\ell+1} \frac{M_B}{M_A} \quad 12.$$

are multipolar tidal polarizability coupling constants. The current analytical knowledge comprises gravitoelectric terms $\ell = 2, 3$ up to next to next leading order (coefficients $\alpha_{1,2}^{(2+,3+)}$) and gravito-magnetic terms up to next to leading order (coefficient $\alpha_1^{(2-)}$).

Taking the Newtonian limit illustrates the meaning of the above formulas:

$$H_{\text{EOB}} \simeq Mc^2 + \frac{\mu}{2}p^2 + \frac{\mu}{2}(A - 1) = Mc^2 + \frac{\mu}{2}p^2 + \frac{\mu}{2}\left(-\frac{2GM}{c^2 r} + \ldots - \frac{\kappa_2^T}{r^6} \right). \quad 13.$$

The constant $\kappa_2^T = \kappa_2^A + \kappa_2^B$ encodes the effect of tidal interactions at leading order. For a large span of EoS, masses in $[1, 2]M_\odot$ and mass ratios in $q \in [1, 2]$, its values are $\kappa_2^T \sim [50, 500]$. A common alternative (but more cumbersome) notation uses the quantities $\Lambda_2^i \equiv 2/3k_2^i(c^2 R_i/GM_i)^5$ with $i \in \{A, B\}$ in place of the κ_2^A and defines

$$\tilde{\Lambda} = \frac{16}{13} \frac{(M_A + 12M_B)M_A^4}{M^5} \Lambda_A + (A \leftrightarrow B). \quad 14.$$

The conservative dynamics described above is complemented by a waveform providing the radiation reaction for the dynamics and the emitted radiation (42). Tidal corrections are introduced also in the waveform (6, 43). At leading order, the stationary phase approximation of the waveform reads

$$h(f) = Af^{-7/6}e^{-i(\Psi_0(x) + \Psi_{\text{tidal}}(x))} = Af^{-7/6}e^{-i(\Psi_0(x) - 39/4\kappa_2^T x^{5/2})}, \quad 15.$$

where $x(f) = (\pi GMf/c^3)^{2/3}$, and $\Psi_0(x)$ is the point-mass phase. Note that the tidal contribution at leading order is again fully determined by κ_2^T. For this reason, the latter (or equivalently $\tilde{\Lambda}$) is the quantity that is best measured from GW observations.

The validity of the EOB description of tides has been tested in the high-frequency regime against long-term NR simulations starting at about 500 Hz and lasting about 10–20 orbits up to merger (39, 44–47). Using the EOB point-mass dynamics as a baseline, the PN expression for A_{tidal} reproduces remarkably well the NR results to within their estimated errors, but it becomes inaccurate in the very last orbits or for large values of κ_2^T. Advanced tidal EOB models have been proposed in References 45 and 47–49 using high-order results from gravitational self-force calculations of tides (TEOBResumS) and in Reference 50 implementing dynamical tides (SEOBNRT). These models currently reproduce a large sample of the available NR waveforms within the numerical uncertainties. In the presence of spins, new tidal contributions arise (51, 52). For example, a rotating star's oblateness creates a deformation in the gravitational field outside the star, which is measured by the quadrupole tensor. This effect, quadratic in the star's self-spin, generates an attractive contribution to the potential that affects the inspiral motion at second PN order $\mathcal{O}(v/c)^4$ (51). Finally, we mention that phenomenological tidal models fitting hybrid EOB and NR data with simple formulas are used for efficient GW analysis (53, 54).

2.3. Gravitational Waves

The formalism described above delivers an accurate GR prediction of the BNS waveform in the complete frequency range of ground-based interferometers, $\sim$10–2,048 Hz. EOB models are the only ones able to predict the GW waveform in the frequency region where PN theory breaks down and NR simulations are neither available nor feasible. Systematic differences between PN approximants at different orders are present already at GW frequencies as low as 50 Hz (6) and can affect the GW parameter estimation at sufficiently high signal-to-noise ratio (SNR). While long-term NR simulations are possible, controlling the phase errors within the subradiant precision over tens to hundreds of orbits remains an open challenge (55). EOB models can be completed in the kilohertz regime with models describing the high-frequency emission from the merger remnant (56). The latter can be inferred only from NR hydrodynamic simulations and usually model the characteristic early-time burst signal (e.g., 57–59). This is summarized in **Figure 1**, which shows the full GW spectrum for a BNS system as well as the time domain waveform in the last few cycles before and after the merger.

Tidal interactions play a key role in determining the late-inspiral and merger dynamics. For example, a binary with two NSs with comparable masses $\sim$1.4$M_\odot$ and low spins performs about $\sim$1,300 revolutions from 30 Hz and merges at $\sim$1.5$-$2 kHz (depending on EoS). In the absence of tidal interactions, the same binary would merge at a frequency three times larger and accumulate a dephasing of 1 radian at $\sim$200 Hz and about 10 radians up to the merger frequency of the BNS.

Under the assumption of Gaussian noise and high SNR, and considering the PN waveform, the measurability of a given parameter is determined from the diagonal elements of the Fisher matrix by integrals of type $I_p = \int d\ln f \gamma(f) f v^p(f)$, where $\gamma(f)df$ is a measure that depends on the noise of the detector and $x \sim (v/c)^2$ (6, 60). Hence, the distribution of information on the GW frequency range is mainly determined by the integrand of I_p (6) (see also **Figure 2**). For a fiducial BNS, the chirp mass (related to I_{-10}) is almost entirely determined by the signal at low frequencies $\lesssim$30 Hz. Information on the symmetric mass ratio (I_{-6}) and the SNR (I_0) is also primarily given by the useful GW cycles below 50 and 100 Hz, respectively. By contrast, the measurability of tidal parameters is related to I_{+10}. Thus, while the total mass can be extracted rather accurately with nontidal templates, capturing the GW phasing above 100 Hz requires tides.
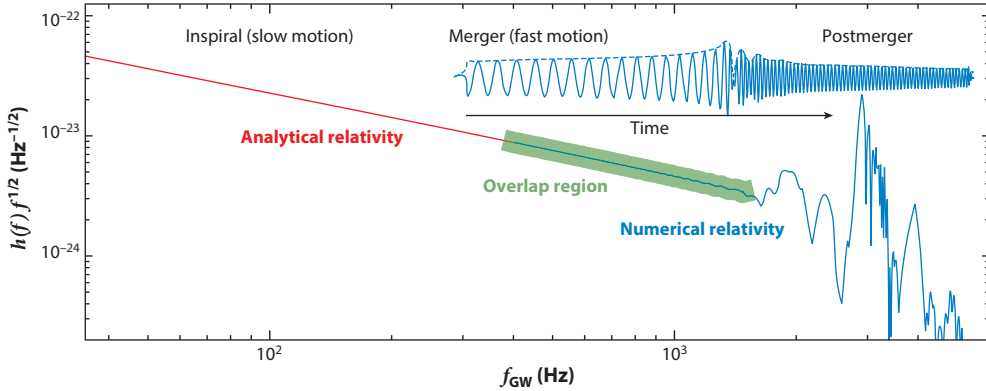
Figure 1

Schematic representation of the complete gravitational wave signal from binary neutron star mergers. The inspiral phase can be well described using the tools of analytical relativity, while the postmerger phase can only be described with numerical relativity. Complete waveform models are constructed by matching the two approaches in the region where both are valid.

A straightforward argument based on the Newtonian equations presented above indicates that the merger dynamics is primarily determined by κ_2^T (45). This expectation has been directly verified to the percent level with more than hundreds of NR simulations (56, 61). For example, the GW frequency at the time of merger can be fitted to the percent level with

$$f_{GW}^{merger} \simeq 2.405 \left(\frac{1 + 1.307 \times 10^{-3}\xi}{1 + 5.001 \times 10^{-3}\xi} \right) \left(\frac{M}{2.8M_\odot} \right) \text{ kHz,} \qquad 16.$$

where $\xi = \kappa_2^T + 3{,}200(1 - 4\nu)$. Similar relations exist for all the relevant dynamical quantities, such as the binding energy, the angular momentum, and the GW luminosity at merger (45, 56, 61). These relations are often called quasi-universal or EoS insensitive because once the quantities are appropriately rescaled by the binary mass and symmetric mass ratio, they are simple functions of the mass ratio and of κ_2^T, the latter of which encodes all the EoS information. It should be noted that even though the errors introduced by the EOB approach are maximum at merger (the moment at which the description of the system as a binary breaks down), the EOB results still agree to within $\lesssim 20\%$ with the NR fitting formulae discussed above.

In the case of GW170817, most of the SNR was accumulated in the frequency range 30–600 Hz, roughly corresponding to the last 1,300 orbits to merge for an equal-mass binary with total mass $M \simeq 2.7M_\odot$. GW170817 is compatible with a BNS system with chirp mass $\mathcal{M} = 1.186(1)M_\odot$, mass ratio $q \in [1, 1.34]$, and $\tilde{\Lambda} \simeq 300$ and smaller than ~ 800 (1, 2, 62). The constraint on $\tilde{\Lambda}$ translates to $\kappa_2^T \lesssim 150$. Among the different waveform approximants used in the analysis (62), EOB models favor slightly larger median values for $\tilde{\Lambda}$ (larger radii) than the others, but all results are compatible at the 90% confidence level. Also, if priors include a lower bound on $\tilde{\Lambda}$ inferred from the interpretation of the EM counterpart, then larger values of $\tilde{\Lambda}$ are favored (63, 64).

The mass ratio and the individual masses for GW170817 are less precisely determined, and there are systematic uncertainties also related to the spin priors (2). Because the tidal parameters are partially degenerate with the mass ratio, these uncertainties also affect the EoS constraints derived from GW170817. When low spin priors (dimensionless NS spins assumed to be $\lesssim 0.05$)
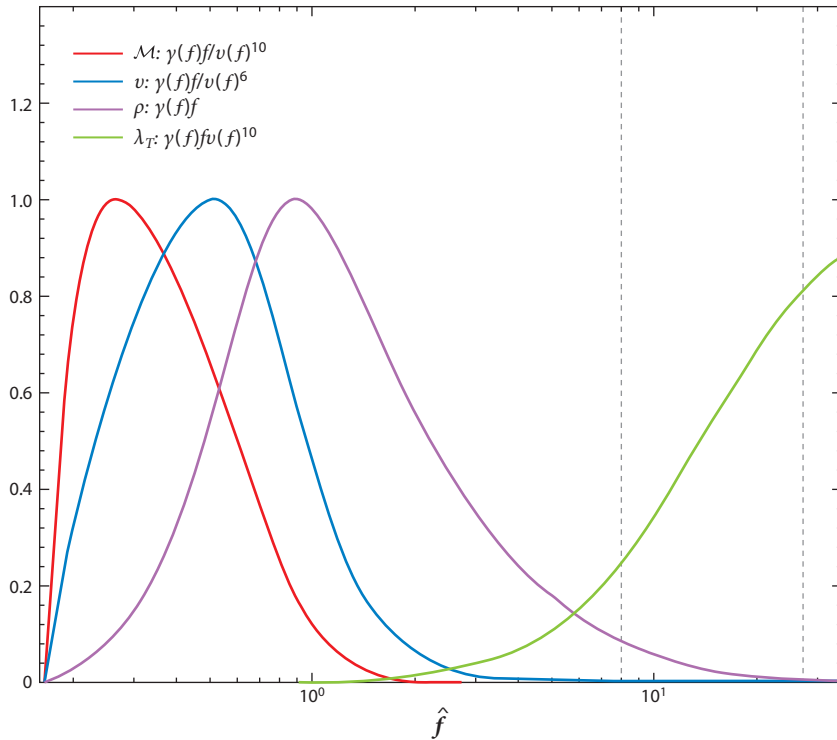
Figure 2

Measurability of the binary chirp mass $\mathcal{M}$, symmetric mass ratio ν, and tidal deformability parameter λ_T (equal to $32M^5\tilde{\Lambda}$ in our notation) as a function of the normalized gravitational wave frequency $\hat{f} = f/f_0$, with $f_0 \simeq 57$ Hz being the frequency at which the signal-to-noise ratio density ρ is at its maximum. The analysis considers one LIGO detector at design sensitivity (`ZERO_DET_high_P` configuration) and $M_A = M_B = 1.4M_\odot$. The rightmost dashed vertical line denotes the contact frequency (Equation 8), while the leftmost dashed vertical line denotes 450 Hz. Figure adapted with permission from Reference 6; © 2012 American Physical Society.

are assumed, the individual radii of the NSs are inferred to be about $R \sim 11$–12 km (65, 66), where the most precise measurement at 90% credible level $R \simeq 11.9 \pm 1.4$ km is obtained with the additional requirement that the EoS must support nonrotating NSs with masses of at least $1.97M_\odot$ (66).

The inspiral signal and tidal phasing can directly constrain regions in the EoS pressure–density diagram (66). The pressure is best constrained at around the maximum density of the NSs in the binary (67), which for the fiducial BNS is $\rho_{max} \simeq 2\rho_0$. Abbott et al. (66) found $P(2\rho_0) = 3.5^{+2.7}_{-1.7} \times 10^{34}$ dyn cm^{-2} at the 90% level.

The merger GW signal was not observed, but the GW frequency at merger can be accurately predicted from the probability distribution of $\tilde{\Lambda}$ using the NR fit (Equation 16). It falls in the range of 1.2–2 kHz (56). Similarly, the peak luminosity is estimated to be larger than 0.1×10^{56} erg s^{-1} (62). The sensitivity of the detectors in August 2017 was insufficient to clearly identify a signal at frequencies $f \gtrsim f_{mrg}$ (68, 69), but if the merger had produced an NS remnant, the main peak frequency of the postmerger signal should have been located at 2.5–3.2 kHz (56).
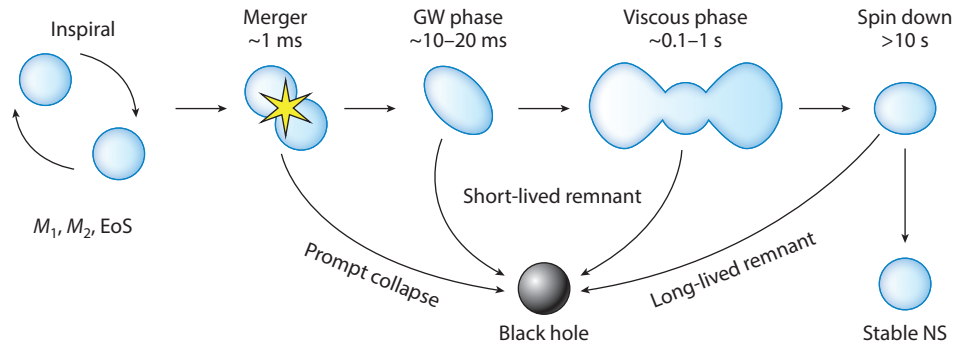
Figure 3

Overview of the different phases in an NS merger and the relative timescales. The inspiral ends with the merger, when the two stars start to fuse together. The early postmerger evolution is entirely driven by hydrodynamics and by GW emission. If the remnant does not collapse within ~10−20 ms, GW losses subside and other physical processes become more important: Angular momentum redistribution (which is due to turbulent viscosity) and neutrino losses operate over a timescale of a tenth of a second to a few seconds. This is also the characteristic timescale for the evolution of the remnant disk. If the remnant does not collapse over a timescale of a few seconds, then it will spin down because of magnetohydrodynamic effects over a possibly much longer timescale of several seconds to a few hours. Abbreviations: EoS, equation of state; GW, gravitational wave; NS, neutron star.

3. MERGER AND POSTMERGER

As the NSs come into contact and the inspiral terminates, the dynamics of the system becomes increasingly complex. Matter is compressed and heated up to extreme densities and temperatures, and new physical effects, such as magnetohydrodynamics (MHD) turbulence and neutrino–matter interactions, become important (Section 3.1) and can affect the outcome of the merger in ways that are not completely understood (Section 3.2). **Figure 3** provides an overview of the BNS dynamics after merger. BH formation might be the immediate outcome of the merger, or it could be delayed by milliseconds to minutes. It is also not excluded that some BNSs might even form stable NS remnants. After a first phase in which GW emission and hydrodynamics play the most important role, GW emission decays, and angular momentum transport due to MHD stresses and neutrino emission and reabsorption takes over. Over longer timescales, if the remnant has not yet collapsed to a BH, the system spins down because of residual GW losses and EM torques.

3.1. Dynamics and Thermodynamics Conditions

During the binary inspiral, the NS matter is assumed to be in cold, neutrinoless, weak equilibrium, and degenerate baryons are the major source of pressure.

Tidal deformation dissipates energy, but the increase in temperature $\Delta T \lesssim 0.1$ MeV and the neutrino losses are marginal up to the final phase of the inspiral (70). Thus, this equilibrium composition is maintained up to merger.

The binary orbital speed at merger can be estimated as $v_{\mathrm{orb}} \simeq \Omega r \simeq \sqrt{GM/(R_A + R_B)}$, and for an equal-mass merger it reads

$$v_{\mathrm{orb}}/c \simeq \sqrt{C} \simeq 0.39 \, (C/0.15)^{1/2}. \qquad 17.$$

Because during the inspiral the GW frequency is approximately twice the orbital frequency, and at leading order its evolution satisfies $\dot{\Omega}_{\mathrm{GW}}^3 \sim (3{,}456/125) \, (G\mathcal{M}_c/c^3)^5 \, \Omega_{\mathrm{GW}}^{11}$, the radial infall velocity

$v_r \simeq 2 \, \Omega \, r \, \dot{\Omega}/(3\Omega^2)$ can be estimated as

$$v_r/c \simeq \frac{192\pi}{15} \frac{G^3 M^3}{c^5 (R_A + R_B)^3} \frac{q}{(1+q)^2}. \qquad 18.$$

For an equal-mass merger, $v_r/c \simeq 0.034(C/0.15)^3$. Since $v_{\mathrm{rad}} \ll v_{\mathrm{orb}}$, the dynamics is primarily dominated by the orbital motion and

$$t_{\mathrm{merger}} \simeq 1 \, / \left(2 f_{\mathrm{GW}}^{\mathrm{contact}}\right) \simeq 1.50 \, \mathrm{ms} \, (M/2.8M_\odot)^{-1/2} \, (C/0.15)^{-3/2} \qquad 19.$$

for NSs of comparable masses. Clearly, more massive binaries and more compact NSs result in faster and more violent mergers. Pieces of matter coming from each of the two NSs slip past each other at the contact interface, and Kelvin–Helmholtz instability occurs. The two NS cores, which initially reside behind this contact interface, fuse over a timescale of a few t_{merger}.

The forming remnant is initially far from hydrodynamical equilibrium: Episodes of (gravity-driven) matter compression and (nuclear-driven and centrifugally driven) expansion follow one another, and the remnant bounces several times. The maximum density and temperature increase immediately after merger as a consequence of matter compression and oscillate because of the bounce dynamics (71). Despite the large relative collision speed, the high speed of sound of matter at nuclear and supranuclear densities ($c_s \gtrsim 0.2c$ for $\rho \gtrsim \rho_0$) prevents the formation of hydrodynamical shocks inside the two coalescing cores. Only at the surface of the massive NS (MNS) can pressure waves steepen into shock waves, which accelerate matter at the edge of the remnant up to mildly relativistic speeds (see Section 4). Thus, matter inside the cores remains cold ($T \lesssim 10\,\mathrm{MeV}$; $s \lesssim 1k_{\mathrm{B}}$/baryon) during the entire merger process. This is clearly visible in **Figure 4**, where the thermodynamic conditions of matter during the merger are presented.

While the densest parts of the cores rotate and fuse, compressed matter at the contact interface is pushed outward. Compression and shear dissipation increase its temperature (up to $T \sim 70-110\,\mathrm{MeV}$; see **Figure 4**), forming a pair of corotating hot spots displaced by an angle of $\sim\pi/2$ with respect to the densest cores (72). This structure survives until the cores have completed their fusion (or until BH formation). At that point, the hot spots have evolved into a hot annulus. The core of the remnant remains relatively cold instead.

Material expelled from the central part of the remnant because of tidal torques or from the collision interface settles into a thick accretion disk, with a typical aspect ratio of $H/R \sim 1/3$ and mass between 0.001 and $0.2M_\odot$. A phenomenological fit in terms of the $\tilde{\Lambda}$ parameter has been proposed and combined with the GW data to derive a new constraint on $\tilde{\Lambda}$ (63, 64, 73). Because of the different temperatures in the tidal tail (cold) and collisional interface (hot), the disk is initially highly nonuniform, as shown in **Figure 4a**. As a consequence of the fast expansion, densities and temperatures drop inside the forming disk. Because the EoS is dominated by nonrelativistic baryons and the expansion proceeds mostly adiabatically, their evolution satisfies $T^3/\rho^2 \sim$ const.

During the core fusion phase, the remnant is characterized by a pronounced ($m = 2$) bar deformation that powers a significant emission of GWs over the first $\sim10-20\,\mathrm{ms}$ after merger and launches spiral waves into the disk. The emission of energy and angular momentum provides a back-reaction that quickly damps the bar mode. Thus, the GW emission is the major driver of the dynamics in the immediate aftermath of the merger. We refer to this phase as the GW-dominated postmerger phase.

The continued action of shocks and spiral waves increases the entropy in the disk and eventually produces an axisymmetric Keplerian disk characterized by a temperature profile that changes smoothly from $\sim10\,\mathrm{MeV}$ (for $\rho \simeq 10^{13}\mathrm{g\,cm^{-3}}$) down to $\sim0.1\,\mathrm{MeV}$ (for $\rho \simeq 10^4\mathrm{g\,cm^{-3}}$), as shown
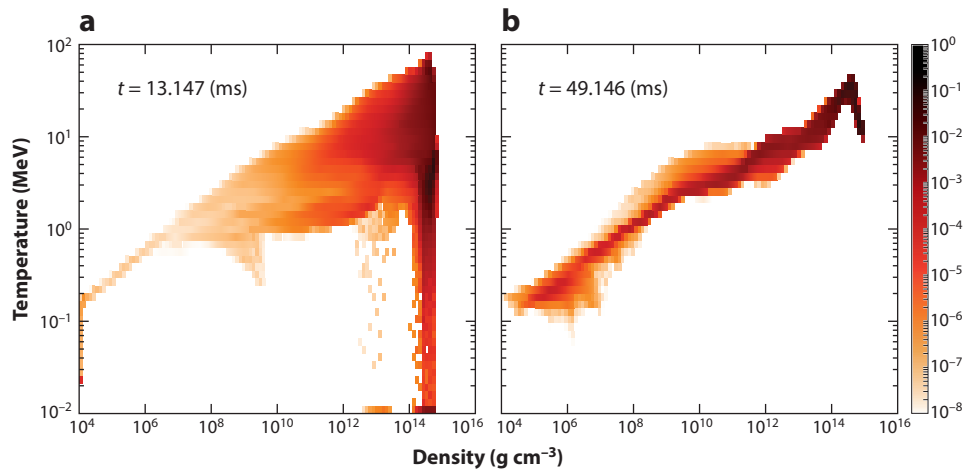
Figure 4

Histograms of the thermodynamic conditions experienced by matter during a binary neutron star merger from an equal-mass merger simulation extending up to 40 ms postmerger and employing the DD2 equation of state. (*a*) Immediately after the merger, when the peak temperatures are reached, matter around and below nuclear saturation density reaches temperatures of several tens of MeV. The neutron star cores are visible as ultra-high-density, low-temperature regions, while the disk forming at lower densities is highly nonhomogeneous. (*b*) At much later times, the two cores have fused into a single one. The rotational dynamics, coupled with the adiabatic expansion, has driven the remnant toward axisymmetric thermodynamic conditions. Animated versions of this figure for a binary simulation employing the SFHo equation of state are available as **Supplemental Figures 1** and **2**. Figure adapted with permission from Reference 71; © 2019 Springer Nature.

in **Figure 4***b*. Correspondingly, the entropy per baryon varies between three and several tens of k_B.

BH formation significantly affects the disk properties. If the central object collapses to a BH, approximately half of the disk mass is swallowed inside the apparent horizon within a dynamical timescale, and the maximum density decreases to a few times 10^{12} g cm^{-3}. Disks hosting a BH at their center are more compact and achieve higher temperatures and entropies ($\Delta s \simeq 2\ k_B$/baryon) than disks hosting an NS remnant (71).

Magnetic fields are not expected to play an important role in the inspiral, but they might affect the postmerger evolution (19, 74). Even weak initial fields can be amplified up to values in excess of 10^{16} Gauss by a number of mechanisms. These include flux freezing and compression, the Kelvin–Helmholtz instability at the collisional interface (75), the magnetorotational instability (19, 74), and magnetic field winding (74).

A crucial question is whether ordered large-scale fields are formed by dynamo processes after the initial amplification. Ordered fields have the potential to power relativistic jets (76, 77) or drive mildly relativistic outflows (78, 79). However, even an unstructured magnetic field can generate magnetic stresses. Because the MHD instabilities known to operate in the merger and postmerger operate on length scales as small as a few tens of meters to centimeters, it is presently impossible to perform fully resolved, global binary NS merger simulations with realistic initial conditions. Extremely high-resolution simulations can resolve the MHD instabilities after merger, but only if the NSs are already endowed with magnetar-strength magnetic fields prior to merger, since this pushes the instabilities to larger scales (19, 75).

Angular momentum transport due to MHD turbulence can be parameterized as an effective α-viscosity. Simulations including a physically motivated prescription for viscosity in GR find that the remnant more quickly becomes axisymmetric, possibly reducing the postmerger GW emission (20, 80). Angular momentum redistribution in the remnant inside the massive NS happens on the following timescale (81):

$$t_{\rm rem} \simeq \alpha^{-1} R_{\rm rem}^2 \, \Omega_{\rm rem} \, c_s^{-2} \simeq 0.56\,{\rm s} \left(\frac{\alpha}{0.001}\right)^{-1} \left(\frac{R_{\rm rem}}{15\,{\rm km}}\right)^2 \left(\frac{\Omega_{\rm rem}}{10^4\,{\rm kHz}}\right) \left(\frac{c_s}{0.2c}\right)^{-2}, \qquad 20.$$

where $\Omega_{\rm rem}$ and c_s are the remnant angular velocity and typical sound speed, respectively. The removal of the differential rotation leads to a more uniformly rotating object and possibly to its gravitational collapse (81). Inside the Keplerian disk, the angular momentum redistribution causes matter accretion (21, 24, 79, 82) on the following timescale:

$$t_{\rm disk} \simeq \alpha^{-1} \left(\frac{H}{R}\right)^{-2} \Omega_{\rm K}^{-1} \simeq 0.78\,{\rm s} \left(\frac{\alpha}{0.02}\right)^{-1} \left(\frac{H/R}{1/3}\right)^{-2} \left(\frac{M_{\rm rem}}{2.5 M_\odot}\right)^{-1/2} \left(\frac{R_{\rm disk}}{100\,{\rm km}}\right)^{3/2}, \qquad 21.$$

where $M_{\rm rem}$ is the mass of the central remnant and $R_{\rm disk}$ is the radial scale of the disk.

At the end of the GW-dominated phase, neutrino emission becomes the most relevant cooling mechanism (14, 83, 84). In particular, hot and dense matter produces neutrinos of all flavors that are eventually emitted to infinity. The typical neutrino mean free path is $\lambda_\nu \simeq (n_{\rm B} \sigma_0 (E_\nu / m_e c^2)^2)^{-1} \simeq 24.6\,{\rm m} (\rho/10^{14} {\rm g\,cm^{-3}})^{-1} (E_\nu / 10\,{\rm MeV})^{-2}$, where $n_{\rm B}$ is the baryon density, $\sigma_0 \simeq 4 G_F^2 \left(m_e c^2\right)^2 / (\pi (\hbar c)^4) \simeq 1.76 \times 10^{-44}\,{\rm cm^2}$ is the typical neutrino cross section scale, and E_ν is the neutrino energy. Assuming $T_{\rm rem} \simeq 20\,{\rm MeV}$ to be the characteristic temperature of a central remnant that has not (yet) collapsed to a BH, a thermal neutrino's ($E_\nu \simeq 3.15\,T_{\rm rem}$) optical depth is $\tau_\nu \simeq R_{\rm rem}/\lambda_\nu = \mathcal{O}(10^4)$. Thus, neutrinos are radiated on the diffusion timescale (85):

$$t_{\rm diff} \simeq \frac{\tau_\nu R_{\rm rem}}{c} \simeq 4.28\,{\rm s} \left(\frac{R_{\rm rem}}{15\,{\rm km}}\right)^{-1} \left(\frac{M_{\rm rem}}{2.5 M_\odot}\right) \left(\frac{T_{\rm rem}}{20\,{\rm MeV}}\right)^2. \qquad 22.$$

Charged current reactions bring neutrinos into thermal and weak equilibrium with matter. As the temperature increases, $\mu_n - \mu_p + \mu_e < 0$ deep inside the remnant, and $\bar\nu_e$ dominate over ν_e, since the latter are suppressed by degeneracy. Antineutrino abundances are expected to be $Y_{\bar\nu_e} \simeq 0.015$, but the impact of trapped neutrinos seems overall marginal (16, 71). Neutrinos' optical depths are much closer to unity inside the disk, so neutrinos with average energies diffuse and stream out within a few milliseconds. These neutrino-cooled disks are locally very close to weak equilibrium with $Y_e \simeq 0.1$ because they regulate themselves to a mildly degenerate state ($\mu_e / k_B T \sim 1-3$) due to the negative feedback of degeneracy on the cooling rate (86).

The decompression and the heating up of cold matter initially in neutrino-less weak equilibrium lead to its leptonization, implying $L_{\bar\nu_e} \gtrsim L_{\nu_e}$, at least during the early postmerger phase. Because free neutrons are abundant, the absorption opacities for ν_e are larger than those for $\bar\nu_e$, while pair processes, responsible for keeping $\nu_{\mu,\tau}$ and their antiparticle in equilibrium, decouple at much larger densities and temperatures inside the remnant—namely, $\rho \gtrsim 10^{13} {\rm g\,cm^{-3}}$ and $T \gtrsim 8\,{\rm MeV}$ (85, 87). Accordingly, BNS simulations including neutrino transport predict the mean neutrino energies at infinity $E_{\nu_e} (\sim 10\,{\rm MeV}) \lesssim E_{\bar\nu_e} (\sim 15\,{\rm MeV}) \lesssim E_{\nu_{\mu,\tau}} (\sim 20\,{\rm MeV})$, with more massive binaries and softer EoSs resulting in higher mean energies (14, 87).

Because of the strong dependence of the cross sections on the incoming neutrino energy, neutrinos with different energies decouple from matter from very different regions. While average-energy ν_e and $\bar\nu_e$ decouple in the disk at densities between a few and several times $10^{11} {\rm g\,cm^{-3}}$,

respectively, low-energy neutrinos decouple at around 10^{13} g cm^{-3} along spheroidal neutrino decoupling surfaces (85, 87). The corresponding large variety of relevant thermodynamic conditions implies the need for a coherent treatment of strong and weak interactions over several orders of magnitude in particle densities and temperatures as well as the need for energy-dependent treatments of neutrino transport in merger simulations.

The role of neutrino oscillations in BNS mergers is largely unexplored. While it is unlikely that neutrino oscillations play a relevant role in the dynamics and fate of the remnant, they might affect the properties of the ejecta by changing the flavor content of the irradiating neutrino fluxes. The fact that electron antineutrinos have the largest luminosities and decouple from smaller radii allows for a new kind of oscillation known as matter–neutrino oscillations to occur a few tens of kilometers above the remnant, possibly affecting the properties of the polar ejecta (e.g., 88, 89). Stability analyses have also shown that neutrino pairs are potentially unstable against fast-flavor conversions immediately above the neutrino decoupling surfaces (90). However, only more detailed calculations using the neutrino quantum kinetics equations (91, 92) and taking into account the collision integral, as well as the angular and energy distributions of neutrinos emerging from the remnant, will properly address the relevance and the impact of neutrino oscillations.

The EoS of NS matter has a clear imprint on the merger dynamics and on the observables. While the low-density part of the nuclear EoS ($\rho \lesssim \rho_0$) is reasonably well known, large uncertainties still affect the high-density part (e.g., 93, 94). These uncertainties concern both the nature of the nucleonic interaction and the relevant thermodynamic degrees of freedom in ultradense environments. In particular, the appearance of new species is expected to decrease the degeneracy of nucleonic matter, lowering the pressure and softening the EoS. These particles include hyperons and nucleonic resonances (e.g., 95) but also significant fractions of pions and muons because of the high temperatures reached inside the remnant (e.g., 96). A QCD phase transition to deconfined quark matter is expected to occur at very high densities (and possibly temperatures), but the onset of this transition as well as its type is still largely unconstrained (97).

During the merger, the appearance of these new degrees of freedom can potentially affect the stability of the remnant, as discussed in Section 3.2.

3.2. Fate of the Remnant

The outcome of BNS mergers depends on the binary parameters and on the (poorly known) NS EoS. In particular, whether and when a BH forms is primarily determined by the total mass of the binary measured at infinite separation $M = M_A + M_B$ and by the maximum mass supported by the EoS for a nonrotating NS $M_{\mathrm{max}}^{\mathrm{TOV}}$ (22). However, finite temperatures and non-beta-equilibrated composition effect, as well as the binary mass ratio and the spins, might also affect the merger outcome.

Sufficiently massive and/or compact binaries form BHs promptly during merger—that is, without experiencing any recoil following the collisions between the stars. For comparable-mass systems, prompt BH formation has been empirically determined to occur if $M \gtrsim M_{\mathrm{thr}} = k_{\mathrm{thr}} M_{\mathrm{max}}^{\mathrm{TOV}}$, with $k_{\mathrm{thr}} = 1.3-1.7$ being an EoS-dependent quantity (98–101). An alternative condition is that prompt BH formation occurs if $\kappa_2^T \lesssim 43-73$ (equivalently if $\tilde{\Lambda} \lesssim 338-386$) (61, 67). The threshold mass for prompt BH formation in unequal-mass binaries is not well constrained, but simulations indicate that M_{thr} is smaller for these binaries (102). Several works have explored the dependency of k_{thr} on the EoS and have shown the existence of EoS-insensitive relations linking k_{thr} to the compactness of a reference $1.6 M_\odot$ NS $C_{1.6}$ predicted by each EoS, or to the compactness of the maximum-mass nonrotating NS C_{max} (100, 101, 103). Prompt BH mergers are commonly thought to be EM-quiet because in most of these cases, all of the matter is engulfed by the BH horizon before photons (or even neutrinos) can escape. For this reason, GW170817 is thought

not to have undergone prompt BH formation (102, 104). However, it is important to emphasize that an EM counterpart is still possible even with prompt BH formation for binaries with large mass ratios (105).

Binaries not undergoing prompt BH formation result in the formation of massive NSs that are at least temporarily supported against gravitational collapse by the fast rotation (14, 81, 98, 99, 106–108). These remnants are classified as supramassive NSs (SMNSs) if $M_{max}^{TOV} \leq M \leq M_{max}^{RNS}$, with M_{max}^{RNS} being the maximum mass predicted by the zero-temperature EoS for a rigidly rotating NS; otherwise, they are classified as hypermassive NSs (HMNSs) (106). HMNSs are thought to be supported by differential rotation, while SMNSs can be supported even after differential rotation has been erased by viscosity. Very-low-mass systems with $M < M_{max}^{TOV}$, if they exist in nature, are expected to form stable MNSs. It is important to emphasize that this classification is based on properties of equilibrium models and ignores the dynamical nature of the remnant. For example, the fate of the remnant depends not only on its total mass but also on the angular momentum, which in turn is set by the stars' radii and spin. Moreover, M_{max}^{RNS} and M_{max}^{TOV} are agnostic to thermal or magnetic effects, which can affect the stability of the remnant in nontrivial ways (73, 109). The fate of SMNSs or HMNSs, especially those with masses close to M_{max}^{RNS}, is unclear: Some HMNSs could lose mass because of viscous processes and remain stable over secular timescales, and, conversely, some SMNSs might collapse because of finite temperature effects (73). We call a remnant short-lived if it collapses during the GW-dominated phase of the evolution, within ∼10–20 ms of the merger (61, 108). Otherwise, we call the remnant long-lived (see **Figure 3**).

Remnants that do not collapse on a timescale of a few seconds—very-long-lived remnants—eventually achieve uniform rotation (73). Afterward, their evolution is driven by the continued emission of GWs due to residual ellipticity and by EM torques until enough angular momentum is lost to trigger their collapse or until the stars settle to nonrotating equilibria. The duration of this phase depends on the magnitude of the dipole component of the magnetic field and on the ellipticity of the remnant. The magnetar model for SGRBs invokes the presence of such very-long-lived remnants to explain the X-ray tails seen in about a third of the SGRBs (110–112). Using these models to fit the X-ray tails of SGRBs provides possible estimates for lifetimes for these remnants that range from tens of seconds to a few hours (112, 113). An important aspect of these models is that the amount of rotational energy that the remnant needs to shed in order to collapse is of the order of a few 10^{52} erg. To be consistent with the inferred EM energetics of SGRB and of GW170817, this energy cannot be primarily radiated in the EM channel. Instead, a significant fraction of this energy has to be radiated as GWs and might be directly detectable for a nearby event (112). It is worth mentioning that there are alternative explanations for the X-ray tails that do not invoke the presence of very-long-lived remnants (e.g., 114).

If detected, the GWs emitted by the merger remnant offer a direct way to observe its fate. However, GW searches for the postmerger signal from GW170817 provided only weak upper limits (68, 69).

The EM data can also be used to constrain the fate of the remnant, although in a model-dependent way. As already mentioned, the very presence of an EM counterpart disfavors the prompt BH formation for the NS merger in GW170817 (63, 102, 104). Whether the merger remnant was hypermassive or supramassive is less clear. The predominant interpretation, attributable to Margalit & Metzger (104), is that GW170817 formed a short-lived remnant. The reason is that, as mentioned above, a long-lived remnant would have injected a few times 10^{52} erg of rotational energy into the ejecta, which can be excluded from observations. Thus, Margalit & Metzger argued that the remnant must have been an HMNS, although, as we have mentioned above, short-lived remnants need not be HMNSs. Because $M_{max}^{RNS} \simeq 1.2 M_{max}^{TOV}$ for most viable NS EoSs (115), assuming that GW170817 was hypermassive implies $M_{max}^{TOV} \lesssim 2.2 M_\odot$ (104).

Other groups have instead interpreted GW170817 in the context of the magnetar model for SGRBs (116–118). To avoid the constraint of Margalit & Metzger, these models invoke a very-long-lived remnant (days to months) endowed with a small dipole magnetic field (116). In this way, only a modest amount of energy is injected into the outflows. This alternative interpretation would imply a larger maximum mass for nonrotating NSs $M_{max}^{TOV} \gtrsim 2.2 M_\odot$, and up to an order of magnitude smaller ejecta masses $\sim 10^{-3} M_\odot$. The reduced ejecta mass estimate arises because, in these models, the energy injected into the outflows by the central remnant supplements the energy due to radioactive heating, so a reduced amount of radioactivity is needed to explain the UV/optical/infrared data (117). Piro et al. (118) found a subthreshold ($\gtrsim 3\sigma$) X-ray flare in the Chandra data for GW170817 at about 160 days after the merger, which they interpret as evidence of a remnant that has not yet collapsed to a BH. However, a follow-up analysis by Hajela et al. (119) did not find evidence of X-ray variability.

3.3. Multimessenger Signatures

The postmerger phase imprints itself in the many multimessenger signatures of BNS mergers. As discussed in more detail in Section 4, neutron-rich material is ejected dynamically as the stars interact (15, 120–123) and on secular timescales after the merger (21, 24, 79, 82, 85, 124, 125). This material undergoes r-process nucleosynthesis and synthesizes heavy elements (12, 15, 83). The radioactive decay of by-products of the r-process powers a transient with a quasi-thermal spectrum, the so-called kilonova (kN) (25), which was observed in association with GW170817.

Even before GW170817, it was thought that NS mergers could generate ultrarelativistic jets and that these jets would power γ-ray flashes (SGRBs) as well as UV/optical afterglows (83, 126). The mechanism for jet launching and the radiative processes responsible for the prompt γ-ray flash are still debated, while the UV/optical afterglow is known to originate because of the interaction between the jet and the interstellar medium (23). Proposed mechanisms for jet launching include magnetic field–mediated energy extraction from a remnant spinning BH (77, 127), magnetized winds from a remnant magnetar (76, 110), or neutrino/antineutrino-powered fireballs (83). In the case of GW170817, a γ-ray flash was detected by both the INTEGRAL and the Fermi satellites with a delay of 1.7 s from the merger (128). Unlike SGRBs seen at cosmological distance, the SGRB in GW170817 was observed off-axis and possibly originated from the wings of a structured jet or from the interaction between the jet and the merger debris (129, 130).

If the remnant avoids gravitational collapse for a sufficient time for all trapped neutrinos to escape, its integrated MeV neutrino luminosity is expected to be a few times 10^{52} erg, comparable to that of a regular core-collapse supernova (73). Unfortunately, this translates to a detection range limited to our galaxy for current and even next-generation neutrino experiments such as SuperK or DUNE (17). Given that the merger rate in our galaxy is one merger every $\mathcal{O}(10^4)$ years, the prospects for detection are not rosy. High-energy GeV/TeV neutrinos and photons generated by nuclear collisions in the SGRB jet or in the remnant magnetosphere (131, 132) might instead be detectable with detectors like IceCube or VERITAS to distances of tens of megaparsecs, depending on the lifetime of the remnant, the binary inclination, and the poorly known physical conditions in the jet, so they are a promising possible "new messenger" from NS mergers.

The postmerger is also the phase with the largest GW luminosity: up to $\sim 0.1 M_\odot c^2 \simeq 2 \times 10^{53}$ erg are radiated over $\sim 10-20$ ms (61, 108). However, most of the GW energy is emitted at high frequency outside the main sensitivity band of the detectors (81, 98, 133, 134), so it will be observable only with third-generation detectors or for very nearby events (58). The postmerger GW spectrum is characterized by the presence of discrete features or peaks. The main one, f_2, is a broad peak at frequencies $\sim 2-4$ kHz (133–136). For a fixed total mass of the system, f_2 is found to
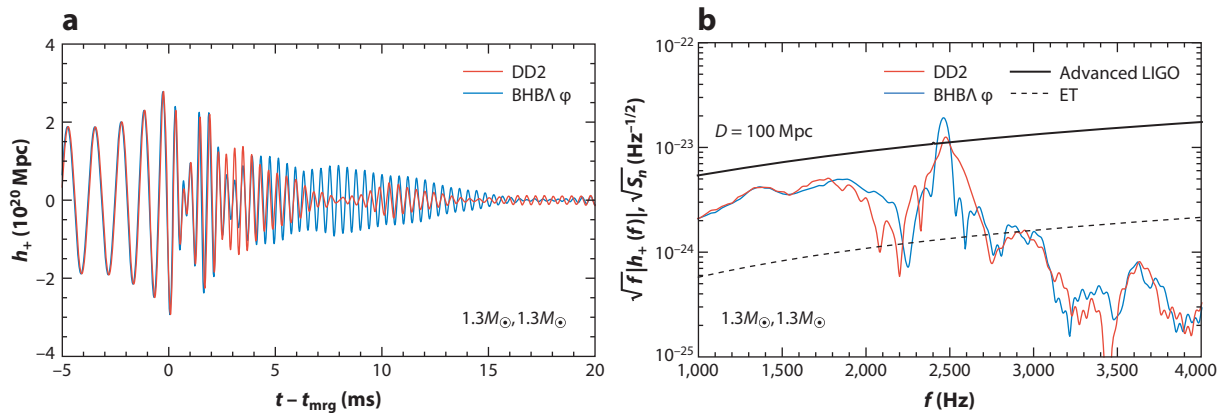
Figure 5

Gravitational wave strain (*a*) and power spectrum (*b*) for two binary neutron star systems with component masses $1.3M_\odot$ and $1.3M_\odot$ simulated with either the DD2 EoS or the BHBΛϕ EoS. The two EoSs are identical at the densities relevant for the inspiral, but they diverge in the postmerger because of the appearance of Λ hyperons in the BHBΛϕ. For more details regarding the simulations, readers are referred to Reference 9. Abbreviation: EoS, equation of state.

correlate with $R_{1.6}$ (81, 133), with only a weak dependency on mass ratio and NS spin (135, 136). A more general quasi-universal relation was found to link f_2 and κ_2^T (or $\tilde{\Lambda}$) in a study by Bernuzzi et al. (57). Both relations could be used to tightly constrain the NS EoS if the postmerger signal is detected (57–59, 81, 137).

Interestingly, even though the densities reached in the postmerger are up to a factor of a few larger than those of the inspiral, these quasi-universal relations imply that the postmerger GW signal should be determined by the lower-density physics that fixes $R_{1.6}$ and κ_2^T. The reason for this is that f_2 is initially set by the orbital frequency of the stars at merger, which is known to depend only on κ_2^T (45). Subsequently, the rates at which angular momentum and binding energy are radiated in GWs are proportional to each other, so f_2 remains roughly constant as the massive NS contracts, at least until the last few cycles before collapse (20, 57, 108, 136). This trend is confirmed in simulations that include second-order phase transitions after merger. In these simulations, the energy liberated by the phase transition boosts the overall GW luminosity but has only a small impact on f_2 (9) (see also **Figure 5**). The only exception is when a strong first-order phase transition is present after merger (11). In such cases, the merger remnant contracts within a single dynamical timescale, so it is the angular momentum and not the angular velocity—as is the case for more gradual contraction due to second-order phase transitions—to be approximately conserved. A strong first-order phase transition could then be revealed by a tension between the κ_2^T inferred from the inspiral signal and that inferred from the postmerger signal (11), assuming that the phase transition does not result in immediate BH formation (10).

4. MATTER EJECTION, KILONOVAE, AND NUCLEOSYNTHESIS

The ejection of neutron-rich material is possibly one of the most important consequences of NS mergers (26). The ejecta are thought to undergo the r-process and produce heavy nuclei, making NS mergers an important, if not dominant, astrophysical site of production for these elements (12). The associated kN signal was observed in GW170817, and because of its quasi-isotropic character, it is considered to be the most promising EM counterpart for future events (25).

For the low-entropy conditions relevant for NS mergers, the outcome of the r-process nucleosynthesis is primarily determined by the electron fraction in the ejecta Y_e (138). If $Y_e \lesssim 0.2$, then the ejecta produce second and third r-process peak elements with relative abundances close to Solar. If $Y_e \gtrsim 0.3$, then the material is not sufficiently neutron rich to produce lanthanides. Instead, first r-process peak elements are produced. The transition between these two outcomes is for $Y_e \simeq 0.25$ and is very sharp. The nucleosynthesis yield changes drastically with Y_e, and the photon opacity in the material also changes by orders of magnitude (139, 140), drastically altering the timescale and the effective blackbody temperature of the kN emission (25). High-Y_e outflows power kNs that peak in the UV/optical bands within a few hours of the merger (the so-called blue kN), while low-Y_e outflows power kNs that peak in the infrared over a timescale of several days (the so-called red kN). In the case of GW170817, both a blue and a red component of the kN were observed, suggesting that the outflow had a broad range of compositions with at least a fraction of the outflow being free of lanthanides.

Part of the outflow is generated on a dynamical timescale: the so-called dynamical ejecta. A fraction of this material is ejected because of tidal torques close to the time of merger (120, 135, 141), especially in the case of very asymmetric binaries. Another fraction is due to shocks generated during and particularly after the merger, when the merged object bounces and launches a shock wave into the forming debris cloud (18, 121–123, 135).

GR merger simulations indicate that the mass of the dynamical ejecta ranges from $10^{-4}M_\odot$ to $10^{-2}M_\odot$ and that it has characteristic velocities of $0.1-0.3c$ (18, 121–123). The tidal ejecta are very neutron rich ($Y_e \sim 0.1$) and cold, while the shocked ejecta are reprocessed to higher Y_e by pair processes and neutrino irradiation from the central remnant, especially at high latitudes. Indeed, because of the larger equatorial densities, neutrino irradiation is more effective close to the remnant rotational axis. Overall, the dynamical ejecta are found to have a broad range of compositions resulting in an r-process nucleosynthesis pattern close to Solar, with some variations depending on the mass ratio (18, 123).

Another component of the outflow, the so-called secular ejecta, is due to winds launched after merger (21, 24, 79, 82, 85, 124, 125, 142). In particular, long-term simulations of neutrino-cooled accretion disks around compact objects indicate that $10-40\%$ of the remnant disk can be unbound over a timescale of a few seconds. Because NS mergers result in the formation of disks with masses up to $\sim 0.2M_\odot$, the secular ejecta are thought to constitute the bulk of the outflow. **Figure 6** shows estimated dynamical and secular ejecta masses from a large collection of NR simulations with microphysics reported previously (123).

Like the dynamical ejecta, the secular ejecta are also launched by different physical mechanisms. At high latitudes, neutrinos from the remnant and the disk drive a moderately high-Y_e wind (82, 85) that unbinds a few $10^{-3}M_\odot$ of material. Close to the equatorial plane, viscous effects transport angular momentum, which causes the disk to spread. Once the accretion rate drops below a critical threshold, neutrino cooling becomes ineffective and the disk thermally expands (86). Subsequently, nuclear recombination of nucleons into alpha particles provides sufficient energy to unbind $\sim 10-20\%$ of the disk and produce outflows with characteristic velocities $\sim 0.1c$ (24, 124, 143). MHD effects can enhance the outflow masses and asymptotic velocities from these disks, especially at early times, and boost the disk ejection fraction to up to $\sim 40\%$ (79, 125). Finally, GR simulations have shown that if the remnant does not collapse to a BH, viscous processes in the remnant can drive even more massive and fast outflows (21, 73, 142).

Overall, the composition of the secular ejecta, and hence the properties of the kN and the nucleosynthesis yield, are found to depend sensitively on the lifetime of the remnant. **Figure 6** shows how the peak magnitudes in optical and infrared wavelengths for different kNs change as a function of the tidal parameter $\tilde{\Lambda}$ (and hence the merger outcome) for the BNS systems
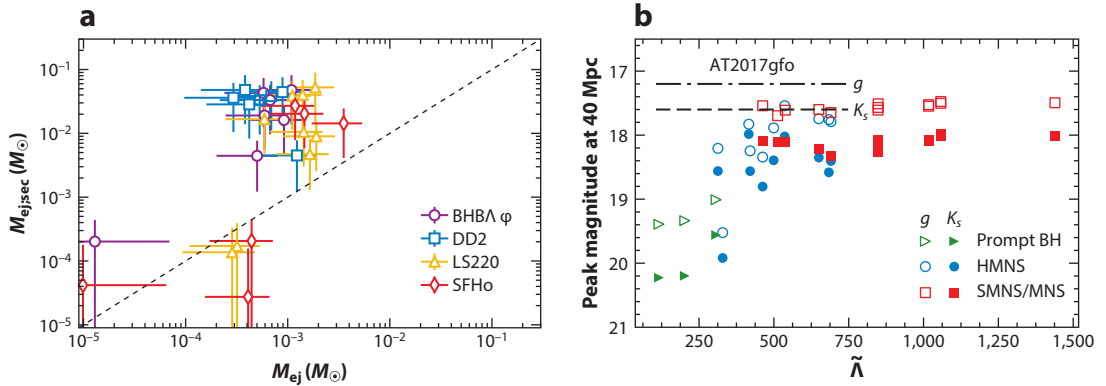
Figure 6

(*a*) Estimated dynamical and secular ejecta masses and (*b*) light curve peak magnitudes in *g* and K_s bands as a function of the tidal parameter $\tilde{\Lambda}$ for the binary neutron star models studied by Radice et al. (123). For comparison, panel *b* also shows the magnitudes of AT2017gfo, the kilonova associated with GW170817. The secular ejecta mass is estimated assuming 20% of the remnant disk to become unbound. For most binaries, the secular component of the outflows dominates. In the case of binaries with compact neutron stars forming BHs promptly or shortly after merger, the kilonova peak magnitudes are dimmer because of the smaller amount of ejecta. The peak in the K_s band always follows the one in the *g* band in time. However, the light curve evolution is much faster and the reddening more significant for smaller $\tilde{\Lambda}$. For the analysis presented in panel *b*, the light curves are computed for an observer at 30°, while the impact of neutrino irradiation from the remnant, which is expected to enhance these differences even more, is not accounted for. Abbreviations: BH, black hole; HMNS, hypermassive neutron star; MNS, massive neutron star; SMNS, supramassive neutron star. Figure adapted with permission from Reference 123; © 2018 The American Astronomical Society.

studied in Reference 123. We remark that this analysis only accounts for the different remnant disk masses—that is, the differences arise because mergers producing short-lived remnants also result in the formation of smaller and more compact disks (71, 73). However, the presence of a long-lived remnant is expected to further affect the EM counterpart and enhance the trend shown in the figure by irradiating the ejecta with neutrinos (24). Nevertheless, the variability of the kN color light curves predicted in these models is significant. For these reasons, kN observations might be promising tools to indirectly probe the outcomes of NS mergers. Unfortunately, the potential of these observations is hindered by the lack of a quantitative understanding of secular mass ejection in mergers. All of the published postmerger simulations adopted somewhat artificial initial conditions (not derived from merger simulations); neglected important physical effects, such as neutrino emission and absorption; assumed axisymmetry; or did not follow the evolution for sufficiently long times.

The kN associated with GW170817 had both a blue and a red component (144; for an alternative interpretation, see Reference 145). The red component has been commonly attributed to low-Y_e secular ejecta because of its inferred large mass ($\sim 0.04 M_\odot$) and low velocity ($\sim 0.1c$). The origins of the blue kN are less clear. Simple light curve fitting and spectroscopy suggest that it might have been powered by $\sim 0.02 M_\odot$ of high-Y_e material expanding with a large velocity $\sim 0.25c$. Some authors have argued that the blue kN might have been powered by dynamical ejecta reprocessed to high Y_e by pair processes and neutrino irradiation (e.g., 146). However, the largest dynamical ejecta mass reported in GR simulations is only $\sim 0.01 M_\odot$ (18). Moreover, only a small fraction of the dynamical ejecta have a sufficiently large Y_e to power a blue kN. More sophisticated multidimensional kN models require somewhat smaller ejecta masses to explain the blue kN in GW170817, but these models are still in some tension with simulations (147, 148). Alternative explanations of the blue kN invoke magnetic effects before or after the merger (78, 79, 149) or

spiral waves launched in the accretion disk by a long-lived massive NS remnant (142). Future observations of the UV emission from NS mergers in the first few hours from the merger might provide additional clues as to which, if any, of these scenarios is correct (78).

While most of the ejecta have velocities $\lesssim 0.4c$, a small fraction of the dynamical ejecta can achieve mildly relativistic velocities up to $\sim 0.8c$ (123, 149–151). This is material that is accelerated as the bounce shock breaks out of the merger debris cloud (123). Some of this material, $\sim 10^{-6}$ to $10^{-5} M_\odot$, expands sufficiently rapidly to prevent neutrons from capturing on seed nuclei, so these ejecta will undergo free neutron decay and produce a UV bump in the light curve on a timescale of 1 h (150). As this fast tail of the ejecta interacts with the interstellar medium, it is also expected to generate a radio synchrotron remnant that is visible on a timescale of months to years after the merger (151, 152). In the case of GW170817, the current radio to X-ray synchrotron emission is consistent with the signal from the deceleration of the SGRB jet (119). However, as the SGRB afterglow decays, it is expected that the ejecta signal might manifest itself as a bump in the radio light curve. The detection of such a signal would confirm that GW170817 produced a massive NS because the acceleration of the outflow to the mildly relativistic velocity required for the radio emission would necessitate the shock produced during the merger bounce (123).

SUMMARY POINTS

1. The dynamics of merging NSs is encoded in the GW signal, which is thus the primary observable for source identification. The low-frequency signal ($\lesssim 50$ Hz) corresponds to the quasi-adiabatic motion and encodes the chirp mass, which was precisely measured for GW170817. Mass ratio and tidal parameters, which need sensitivity at high frequency and precise tidal templates to be well measured, are more uncertain. The early post-merger dynamics has a characteristic transient signal at kilohertz frequencies that can be computed with NR simulations. While full-spectrum models are becoming available, both merger and postmerger were not observed in GW170817.

2. GW signals from inspiraling NSs can be used to constrain the EoS of matter at up to $\rho \sim 2\rho_0$. The most robust constraint available to date from GW170817 is that the tidal parameter $\tilde{\Lambda}$ was smaller than 800 at the 90% confidence level. More precise constraints on the deformability of the stars, the EoS, and the radii of NSs are available but are, to some extent, model and prior dependent.

3. The postmerger phase probes even higher densities and temperatures of tens of to a hundred MeV. However, postmerger GWs are expected to be emitted predominantly at frequencies of $2-4\,\text{kHz}$, outside the sensitivity band of current GW observatories. The nondetection of a postmerger for GW170817 is not constraining for any realistic postmerger model.

4. High-mass BNS mergers result in prompt BH formation. Lower-mass systems form massive NSs that are at least temporarily supported by centrifugal forces against collapse, or even stable NSs. These different outcomes are imprinted in the characteristics of the EM counterparts (or lack thereof). In the case of GW170817, most models favor the formation of a remnant surviving for up to a second and disfavor prompt BH formation or very-long-lived remnants. Alternative outcomes are not completely ruled out: Prompt BH formation might still be compatible with the observations if the mass ratio of the binary was sufficiently large, and the presence of a long-lived remnant might have been hidden if its dipolar magnetic field was sufficiently weak.

5. BNS mergers produce multimessenger signals in addition to GWs, including neutrinos and EM radiation over a broad spectrum of energies. The detection of GRB170817A, an SGRB associated with GW170817, confirmed that compact mergers are central engines of SGRBs. The jet-launching mechanism and its relation with the merger dynamics are still debated.

6. Neutron-rich ejecta from NS mergers synthesize r-process elements and power bright EM transients known as kilonovae (kN). BNS mergers eject matter on different timescales (dynamical and secular) and through different mechanisms (e.g., tidal torques, shocks, nuclear recombination). The kN observed in GW170817 confirms this overall picture and suggests that BNS mergers are an important site of production for r-process elements. However, the origin of the outflows in GW170817 is still debated, especially in connection with the UV/optical "blue" component of the kN that was detected on the first day from the merger. The presence of such a component testifies to the importance of weak reactions in setting the composition of the ejecta.

FUTURE ISSUES

1. How can high-precision measurements of individual stars' masses, spins, and tidal parameters be made? As GW observatories become more sensitive and more NS mergers are detected, waveform systematic effects will dominate over statistical uncertainties. High-fidelity inspiral waveform models capturing the internal dynamics of the stars are needed, but such models require both analytical improvements and higher-quality, longer NR simulations than those that are presently available.

2. What are the relevant thermodynamic degrees of freedom for the description of matter in merging BNSs? The formation of muons and pions, and possibly of hyperons, as well as the appearance of QCD phase transitions and their observable consequences, needs to be studied extensively in simulations. On the one hand, the development of new microphysical EoS frameworks and the calculation of the associated weak interaction rates are required. On the other hand, high-resolution BNS merger simulations with spectral neutrino transport are needed to quantify these effects.

3. What was the origin of the blue component of the kN in GW170817? Do NS mergers produce all three r-process peak elements? Observations show that the outflows from GW170817 must have been sufficiently neutron rich to produce lanthanides, but there is no direct evidence of the production of higher-atomic-mass-number elements, such as gold. Different models have been proposed to explain the EM observations that predict different merger outcomes and nucleosynthesis yields. Early-epoch observations of future events might help to distinguish between these possibilities. Ultimately, ab initio simulations are needed to provide context and to constrain the models used to interpret the EM counterpart on the basis of the information provided by the GW data.

4. What was the fate of the BNS progenitor to GW170817? There are no self-consistent simulations including inspiral, merger, and postmerger evolution that span all relevant timescales and that include all physical processes known to be important. Extant studies suggest that the outcome of the merger is imprinted in the EM and GW signals.

However, because of the lack of quantitative models, it is not presently possible to confidently constrain the merger outcome of GW170817.

5. How do the secular ejecta properties depend on the binary parameters? Merger simulations indicate that the structure and mass of the postmerger remnant are sensitive to binary parameters and EoSs. However, extant long-term postmerger simulations only have considered a handful of idealized initial conditions. Thus, it is not clear how the diversity of postmerger configurations is reflected in the EM counterpart. For example, will secular winds entrain a roughly constant portion of the disk, or will massive disks evolve in a qualitatively different way depending on the disk mass?

6. What is the impact of neutrino irradiation and neutrino oscillations on EM counterparts and nucleosynthesis? Neutrino matter interactions play a crucial role in determining the composition of the outflows and, hence, the nucleosynthesis yields and the EM emissions of BNS mergers. However, on the one hand, extant simulations employ crude approximations to neutrino transport, with the state of the art being gray moment schemes. On the other hand, neutrino opacities in dense matter at the conditions relevant for mergers are still not known in a systematic way. Finally, the impact of neutrino oscillations on the observables is still unclear.

DISCLOSURE STATEMENT

The authors are not aware of any affiliations, memberships, funding, or financial holdings that might be perceived as affecting the objectivity of this review.

ACKNOWLEDGMENTS

LITERATURE CITED

1. Abbott BP, et al. *Phys. Rev. Lett.* 119:161101 (2017)
2. Abbott BP, et al. *Phys. Rev. X* 9:011001 (2019)
3. Abbott BP, et al. *Astrophys. J. Lett.* 848:L12 (2017)
4. Abbott BP, et al. *Living Rev. Rel.* 21:3 (2018)
5. Hinderer T, Lackey BD, Lang RN, Read JS. *Phys. Rev. D* 81:123016 (2010)
6. Damour T, Nagar A, Villain L. *Phys. Rev. D* 85:123007 (2012)
7. Del Pozzo W, et al. *Phys. Rev. Lett.* 111:071101 (2013)
8. Sekiguchi Y, Kiuchi K, Kyutoku K, Shibata M. *Phys. Rev. Lett.* 107:211101 (2011)
9. Radice D, et al. *Astrophys. J. Lett.* 842:L10 (2017)
10. Most ER, et al. *Phys. Rev. Lett.* 122:061101 (2019)
11. Bauswein A, et al. *Phys. Rev. Lett.* 122:061102 (2019)
12. Cowan JJ, et al. arXiv:1901.01410 [astro-ph.HE] (2019)
13. Bejger M, et al. *Astron. Astrophys.* 431:297 (2005)
14. Sekiguchi Y, Kiuchi K, Kyutoku K, Shibata M. *Phys. Rev. Lett.* 107:051102 (2011)
15. Wanajo S, et al. *Astrophys. J. Lett.* 789:L39 (2014)
16. Foucart F, et al. *Phys. Rev. D* 93:044019 (2016)
17. Palenzuela C, et al. *Phys. Rev. D* 92:044045 (2015)
18. Sekiguchi Y, et al. *Phys. Rev. D* 93:124046 (2016)

19. Kiuchi K, Kyutoku K, Sekiguchi Y, Shibata M. *Phys. Rev. D* 97:124039 (2018)
20. Radice D. *Astrophys. J. Lett.* 838:L2 (2017)
21. Fujibayashi S, et al. *Astrophys. J.* 860:64 (2018)
22. Shibata M. *Numerical Relativity*. Singapore: World Scientific (2016)
23. Kumar P, Zhang B. *Phys. Rep.* 561:1 (2014)
24. Fernández R, Metzger BD. *Annu. Rev. Nucl. Part. Sci.* 66:23 (2016)
25. Metzger BD. *Living Rev. Rel.* 23:1 (2020)
26. Shibata M, Hotokezaka K. *Annu. Rev. Nucl. Part. Sci.* 69:41 (2019)
27. Blanchet L. *Living Rev. Rel.* 17:2 (2014)
28. Buonanno A, Damour T. *Phys. Rev. D* 59:084006 (1999)
29. Damour T, Nagar A. *Phys. Rev. D* 81:084016 (2010)
30. Damour T. *Fundam. Theor. Phys.* 177:111 (2014)
31. Damour T. 1983. Gravitational radiation and the motion of compact bodies. In *Gravitational Radiation*, ed. N Deruelle, T Piran, pp. 59–144. Amsterdam: North-Holland
32. Damour T, Soffel M, Xu C. *Phys. Rev. D* 45:1017 (1992)
33. Damour T, Nagar A. *Phys. Rev. D* 80:084035 (2009)
34. Hinderer T. *Astrophys. J.* 677:1216 (2008)
35. Binnington T, Poisson E. *Phys. Rev. D* 80:084018 (2009)
36. Ho WCG, Lai D. *Mon. Not. R. Astron. Soc.* 308:153 (1999)
37. Pons JA, et al. *Phys. Rev. D* 65:104021 (2002)
38. Steinhoff J, Hinderer T, Buonanno A, Taracchini A. *Phys. Rev. D* 94:104028 (2016)
39. Bernuzzi S, Nagar A, Thierfelder M, Brugmann B. *Phys. Rev. D* 86:044030 (2012)
40. Damour T, Jaranowski P, Schäfer G. *Phys. Rev. D* 91:084024 (2015)
41. Bini D, Damour T, Faye G. *Phys. Rev. D* 85:124034 (2012)
42. Damour T, Iyer BR, Nagar A. *Phys. Rev. D* 79:064004 (2009)
43. Banihashemi B, Vines J. arXiv:1805.07266 [gr-qc] (2018)
44. Baiotti L, et al. *Phys. Rev. D* 84:024017 (2011)
45. Bernuzzi S, Nagar A, Dietrich T, Damour T. *Phys. Rev. Lett.* 114:161103 (2015)
46. Dietrich T, Hinderer T. *Phys. Rev. D* 95:124006 (2017)
47. Akcay S, et al. *Phys. Rev. D* 99:044051 (2019)
48. Nagar A, et al. *Phys. Rev. D* 98:104052 (2018)
49. Nagar A, et al. *Phys. Rev. D* 99:044007 (2019)
50. Hinderer T, et al. *Phys. Rev. Lett.* 116:181101 (2016)
51. Poisson E. *Phys. Rev. D* 57:5287 (1998)
52. Pani P, Gualtieri L, Maselli A, Ferrari V. *Phys. Rev. D* 92:024010 (2015)
53. Dietrich T, Bernuzzi S, Tichy W. *Phys. Rev. D* 96:121501 (2017)
54. Kawaguchi K, et al. *Phys. Rev. D* 97:044044 (2018)
55. Bernuzzi S, Dietrich T. *Phys. Rev. D* 94:064062 (2016)
56. Breschi M, et al. *Phys. Rev. D* 100:104029 (2019)
57. Bernuzzi S, Dietrich T, Nagar A. *Phys. Rev. Lett.* 115:091101 (2015)
58. Chatziioannou K, et al. *Phys. Rev. D* 96:124035 (2017)
59. Easter PJ, et al. *Phys. Rev. D* 100:043005 (2019)
60. Cutler C, Flanagan EE. *Phys. Rev. D* 49:2658 (1994)
61. Zappa F, et al. *Phys. Rev. Lett.* 120:111101 (2018)
62. Abbott BP, et al. *Phys. Rev. X* 9:031040 (2019)
63. Radice D, Perego A, Zappa F, Bernuzzi S. *Astrophys. J. Lett.* 852:L29 (2018)
64. Radice D, Dai L. *Eur. Phys. J. A* 55:50 (2019)
65. De S, et al. *Phys. Rev. Lett.* 121:091102 (2018). Erratum. *Phys. Rev. Lett.* 121:259902 (2018)
66. Abbott BP, et al. *Phys. Rev. Lett.* 121:161101 (2018)
67. Agathos M, et al. *Phys. Rev. D* 101:044006 (2020)
68. Abbott BP, et al. *Astrophys. J. Lett.* 851:L16 (2017)
69. Abbott BP, et al. *Astrophys. J.* 875:160 (2019)

70. Lai D. *Mon. Not. R. Astron. Soc.* 270:611 (1994)
71. Perego A, Bernuzzi S, Radice D. *Eur. Phys. J. A* 55:124 (2019)
72. Kastaun W, Ciolfi R, Giacomazzo B. *Phys. Rev. D* 94:044060 (2016)
73. Radice D, Perego A, Bernuzzi S, Zhang B. *Mon. Not. R. Astron. Soc.* 481:3670 (2018)
74. Duez MD, Liu YT, Shapiro SL, Shibata M. *Phys. Rev. D* 73:104015 (2006)
75. Kiuchi K, et al. *Phys. Rev. D* 92:124034 (2015)
76. Bucciantini N, Metzger BD, Thompson TA, Quataert E. *Mon. Not. R. Astron. Soc.* 419:1537 (2012)
77. Ruiz M, Lang RN, Paschalidis V, Shapiro SL. *Astrophys. J. Lett.* 824:L6 (2016)
78. Metzger BD, Thompson TA, Quataert E. *Astrophys. J.* 856:101 (2018)
79. Fernández R, et al. *Mon. Not. R. Astron. Soc.* 482:3373 (2019)
80. Shibata M, Kiuchi K. *Phys. Rev. D* 95:123003 (2017)
81. Hotokezaka K, et al. *Phys. Rev. D* 88:044026 (2013)
82. Miller JM, et al. *Phys. Rev. D* 100:023008 (2019)
83. Eichler D, Livio M, Piran T, Schramm DN. *Nature* 340:126 (1989)
84. Rosswog S, Liebendoerfer M. *Mon. Not. R. Astron. Soc.* 342:673 (2003)
85. Perego A, et al. *Mon. Not. R. Astron. Soc.* 443:3134 (2014)
86. Beloborodov AM. *AIP Conf. Proc.* 1054:51 (2008)
87. Endrizzi A, et al. *Eur. Phys. J. A* 56:15 (2020)
88. Zhu YL, Perego A, McLaughlin GC. *Phys. Rev. D* 94:105006 (2016)
89. Tian JY, Patwardhan AV, Fuller GM. *Phys. Rev. D* 96:043001 (2017)
90. Wu MR, Tamborra I, Just O, Janka HT. *Phys. Rev. D* 96:123015 (2017)
91. Volpe C. *Int. J. Mod. Phys. E* 24:1541009 (2015)
92. Richers SA, McLaughlin GC, Kneller JP, Vlasenko A. *Phys. Rev. D* 99:123014 (2019)
93. Hebeler K, Lattimer JM, Pethick CJ, Schwenk A. *Astrophys. J.* 773:11 (2013)
94. Oertel M, Hempel M, Klähn T, Typel S. *Rev. Mod. Phys.* 89:015007 (2017)
95. Vidana I, et al. *EPL* 94:11002 (2011)
96. Fore B, Reddy S. arXiv:1911.02632 [astro-ph.HE] (2019)
97. Busza W, Rajagopal K, van der Schee W. *Annu. Rev. Nucl. Part. Sci.* 68:339 (2018)
98. Shibata M, Taniguchi K, Uryu K. *Phys. Rev. D* 71:084021 (2005)
99. Shibata M, Taniguchi K. *Phys. Rev. D* 73:064027 (2006)
100. Hotokezaka K, et al. *Phys. Rev. D* 83:124008 (2011)
101. Bauswein A, Baumgarte TW, Janka HT. *Phys. Rev. Lett.* 111:131101 (2013)
102. Bauswein A, Just O, Janka HT, Stergioulas N. *Astrophys. J. Lett.* 850:L34 (2017)
103. Köppel S, Bovard L, Rezzolla L. *Astrophys. J. Lett.* 872:L16 (2019)
104. Margalit B, Metzger BD. *Astrophys. J. Lett.* 850:L19 (2017)
105. Kiuchi K, Kyutoku K, Shibata M, Taniguchi K. *Astrophys. J.* 876:L31 (2019)
106. Baumgarte TW, Shapiro SL, Shibata M. *Astrophys. J. Lett.* 528:L29 (2000)
107. Rosswog S, Davies MB. *Mon. Not. R. Astron. Soc.* 334:481 (2002)
108. Bernuzzi S, et al. *Phys. Rev. D* 94:024023 (2016)
109. Kaplan JD, et al. *Astrophys. J.* 790:19 (2014)
110. Zhang B, Meszaros P. *Astrophys. J. Lett.* 552:L35 (2001)
111. Lasky PD, et al. *Phys. Rev. D* 89:047302 (2014)
112. Fan YZ, Wu XF, Wei DM. *Phys. Rev. D* 88:067304 (2013)
113. Ravi V, Lasky PD. *Mon. Not. R. Astron. Soc.* 441:2433 (2014)
114. Oganesyan G, et al. arXiv:1904.08786 [astro-ph.HE] (2019)
115. Breu C, Rezzolla L. *Mon. Not. R. Astron. Soc.* 459:646 (2016)
116. Ai S, et al. *Astrophys. J.* 860:57 (2018)
117. Li SZ, Liu LD, Yu YW, Zhang B. *Astrophys. J. Lett.* 861:L12 (2018)
118. Piro L, et al. *Mon. Not. R. Astron. Soc.* 483:1912 (2019)
119. Hajela A, et al. *Astrophys. J. Lett.* 886:L17 (2019)
120. Rosswog S, et al. *Astron. Astrophys.* 341:499 (1999)
121. Hotokezaka K, et al. *Phys. Rev. D* 87:024001 (2013)

122. Bauswein A, Goriely S, Janka HT. *Astrophys. J.* 773:78 (2013)
123. Radice D, et al. *Astrophys. J.* 869:130 (2018)
124. Lee WH, Ramirez-Ruiz E, López-Cámara D. *Astrophys. J. Lett.* 699:L93 (2009)
125. Siegel DM, Metzger BD. *Phys. Rev. Lett.* 119:231102 (2017)
126. Berger E. *Annu. Rev. Astron. Astrophys.* 52:43 (2014)
127. Blandford RD, Znajek RL. *Mon. Not. R. Astron. Soc.* 179:433 (1977)
128. Abbott BP, et al. *Astrophys. J. Lett.* 848:L13 (2017)
129. Lazzati D, et al. *Phys. Rev. Lett.* 120:241103 (2018)
130. Xie X, Zrake J, MacFadyen A. *Astrophys. J.* 863:58 (2018)
131. Murase K, Nagataki S. *Phys. Rev. Lett.* 97:051101 (2006)
132. Fang K, Metzger BD. *Astrophys. J.* 849:153 (2017)
133. Bauswein A, Janka HT. *Phys. Rev. Lett.* 108:011101 (2012)
134. Rezzolla L, Takami K. *Phys. Rev. D* 93:124051 (2016)
135. Dietrich T, et al. *Phys. Rev. D* 95:024029 (2017)
136. Dietrich T, Bernuzzi S, Ujevic M, Tichy W. *Phys. Rev. D* 95:044045 (2017)
137. Tsang KW, Dietrich T, Van Den Broeck C. *Phys. Rev. D* 100:044047 (2019)
138. Lippuner J, Roberts LF. *Astrophys. J.* 815:82 (2015)
139. Tanaka M, Hotokezaka K. *Astrophys. J.* 775:113 (2013)
140. Kasen D, Badnell NR, Barnes J. *Astrophys. J.* 774:25 (2013)
141. Radice D, et al. *Mon. Not. R. Astron. Soc.* 460:3255 (2016)
142. Nedora V, et al. *Astrophys. J. Lett.* 886:L30 (2019)
143. Fahlman S, Fernández R. *Astrophys. J. Lett.* 869:L3 (2018)
144. Villar VA, et al. *Astrophys. J. Lett.* 851:L21 (2017)
145. Waxman E, Ofek EO, Kushnir D, Gal-Yam A. *Mon. Not. R. Astron. Soc.* 481:3423 (2018)
146. Nicholl M, et al. *Astrophys. J. Lett.* 848:L18 (2017)
147. Perego A, Radice D, Bernuzzi S. *Astrophys. J. Lett.* 850:L37 (2017)
148. Kawaguchi K, Shibata M, Tanaka M. *Astrophys. J. Lett.* 865:L21 (2018)
149. Radice D, et al. *Astrophys. J. Lett.* 869:L35 (2018)
150. Metzger BD, Bauswein A, Goriely S, Kasen D. *Mon. Not. R. Astron. Soc.* 446:1115 (2015)
151. Hotokezaka K, et al. *Astrophys. J.* 867:95 (2018)
152. Nakar E, Piran T. *Nature* 478:82 (2011)